

DIRECT ELECTRICAL IMPEDANCE TOMOGRAPHY FOR NONSMOOTH CONDUCTIVITIES

K ASTALA, J L MUELLER, A PERÄMÄKI, L PÄIVÄRINTA AND S SILTANEN

ABSTRACT. A new reconstruction algorithm is presented for EIT in dimension two, based on the constructive uniqueness proof given by Astala and Päivärinta in [*Ann. of Math.* **163** (2006)]. The method is non-iterative, provides a noise-robust solution of the full nonlinear EIT problem, and applies to more general conductivities than previous approaches. In particular, the new algorithm applies to piecewise smooth conductivities. Reconstructions from noisy and non-noisy simulated data from conductivity distributions representing a cross-sections of a chest and a layered medium such as stratified flow in a pipeline are presented. The results suggest that the new method can recover useful and reasonably accurate EIT images from data corrupted by realistic amounts of measurement noise. In particular, the dynamic range in medium-contrast conductivities is reconstructed remarkably well.

Version 25 (submitted), August 20, 2010

1. INTRODUCTION

The aim of electrical impedance tomography (EIT) is to reconstruct the conductivity distribution inside an unknown physical body from electric boundary measurements. The reconstruction task is a nonlinear and ill-posed inverse problem. Applications of EIT include medical imaging, nondestructive testing, geophysical prospection and industrial process monitoring. See [21] for a general introduction to EIT.

We present a new computational EIT algorithm in dimension two based on the constructive uniqueness proof given by Astala and Päivärinta in [4, 5]. Our method is non-iterative, provides a noise-robust solution of the full nonlinear EIT problem, and assumes no regularity in the conductivity distribution contrary to previous direct EIT algorithms in the literature. In particular, our method is applicable to the class of piecewise smooth conductivities. This class is important since it describes the conductivity distribution in the human body, as well as those arising in process tomography, such as stratified media in a pipeline. The 2-D case considered here is applicable to reconstruction of a cross-section of a pipeline or a human chest, for example.

The mathematical model of EIT is the inverse conductivity problem of Calderón [20]. We restrict our discussion here to the following two-dimensional setting. Let $\Omega \subset \mathbb{R}^2$ be the unit disc and let $\sigma : \Omega \rightarrow (0, \infty)$ be an essentially bounded

measurable function satisfying $\sigma(x) \geq c > 0$ for almost every $x \in \Omega$. Let $u \in H^1(\Omega)$ be the unique solution to

$$(1.1) \quad \nabla \cdot \sigma \nabla u = 0 \text{ in } \Omega,$$

$$(1.2) \quad u|_{\partial\Omega} = \phi \in H^{1/2}(\partial\Omega).$$

The inverse conductivity problem is to recover σ from the voltage-to-current density map

$$\Lambda_\sigma : \phi \mapsto \sigma \frac{\partial u}{\partial \nu} \Big|_{\partial\Omega},$$

also called the Dirichlet-to-Neumann (DN) map. Here ν is the unit outer normal to the boundary.

Our reconstruction method is based on unique complex geometric optics (CGO) solutions u_1 and u_2 of the conductivity equations

$$(1.3) \quad \nabla \cdot \sigma \nabla u_1(\cdot, k) = 0, \quad \nabla \cdot \sigma^{-1} \nabla u_2(\cdot, k) = 0,$$

where k is a complex parameter and the solutions have asymptotic behaviour $u_1 \sim e^{ikz}$ and $u_2 \sim ie^{ikz}$ when $|z| \rightarrow \infty$. To define these global solutions we have set $\sigma(z) \equiv 1$ outside Ω . In particular, this makes the CGO solutions harmonic in $\mathbb{R}^2 \setminus \Omega$. The exponential behaviour of the CGO solutions is used for constructing a nonlinear Fourier analysis for the inverse conductivity problem, and k can be thought of as a frequency-domain variable.

The reconstruction procedure consists of these three steps:

- (i) **Recover traces of CGO solutions at the boundary $\partial\Omega$ from the DN map by solving the boundary integral equation given in [5].** The exponential ill-posedness of the EIT problem shows up in this step. We present a new regularized real-linear solution method for the integral equation. The effect of measurement noise is abated by restricting the computation to the disc $|k| < R$, where the truncation radius $R > 0$ depends on the measurement noise level (smaller noise allows the use of larger R). In analogy to linear Fourier transform terminology, we will call R the *low-pass cutoff frequency*.
- (ii) **Compute approximate values of CGO solutions inside the unit disc using the *low-pass transport matrix*.** Being harmonic outside Ω , the CGO solutions are determined in $\mathbb{R}^2 \setminus \overline{\Omega}$ by their traces at the boundary $\partial\Omega$. Furthermore, the values of the CGO solutions inside Ω are connected to their values outside Ω through certain Beltrami equations that form a 2×2 linear system. The coefficient matrix for that system on the disk $|k| < R$ is referred to as the low-pass transport matrix.
- (iii) **Reconstruct the conductivity.** The approximate conductivity is computed from the recovered values of the CGO solutions inside Ω using differentiation and simple algebra. Numerical implementation of the derivatives is stable due to smoothing provided by the nonlinear low-pass filtering in Step (ii) above.

We remark that there is no smoothness or continuity assumption on the conductivity, and the method solves the full nonlinear EIT problem in an explicitly regularized fashion directly with no iterations. Further, reconstruction at a given point $z \in \Omega$ is independent from the reconstruction at any other point, enabling region-of-interest imaging and trivial parallelization of the algorithm.

Computationally the most demanding part of the reconstruction method is the evaluation of the low-pass transport matrix in Step (ii). The Beltrami equation solver introduced in [8] could be modified and used here but it is rather slow. The computation time can be significantly reduced, and acceptable computation times achieved, using the fast Beltrami equation solver introduced in [36]. We note that numerical solution of Beltrami equations is discussed also in [29, 25], but with asymptotic conditions not suitable for the present work.

For simplicity we restrict here to the special case of Ω being the unit disc, but this is not a serious loss of generality. The method can be modified to apply to any simply connected plane domain with Lipschitz boundary.

Let us review the history of CGO-based results on the inverse conductivity problem. Calderón solved in [20] a linearized version of the question. Unique determination of an infinitely smooth isotropic conductivity from the DN map in dimension $n \geq 3$ was shown in [70]. This result has been extended to conductivities having $\frac{3}{2}$ derivatives in [62] (see also the refinement [16]), and in [33] for conductivities having $C^{1,\alpha}$ -smooth conormal singularities on submanifolds. Constructive reconstruction algorithms for infinite-precision EIT data in three dimensions were proposed in [59, 61]; see [12, 14, 15, 24] for 3D CGO-based algorithms for finite precision data.

Many algorithms using CGO solutions make use of a D-bar, or $\bar{\partial}$, equation for the computation of these solutions, especially in dimension two. The unique identifiability of isotropic conductivities from infinite-precision data was proven in [60] for twice differentiable conductivities. Reduction to one derivative was provided in [17], and Calderón's original L^∞ question was answered in [4]. A numerical EIT algorithm was introduced in [64], based on [60] but applicable to finite-precision data, regularized using Born approximation and a nonlinear low-pass filter. That D-bar algorithm has been applied to simulated data in [49, 56, 57, 65, 66] and to laboratory and *in vivo* human data in [42, 43, 58, 26], resulting in useful reconstructions of both smooth and piecewise smooth conductivities. A reconstruction method based on [17] is given in [46, 47, 53]. Also, Calderón's original linearized method has been applied to experimental data in dimension two in [13].

The question of stability of the inverse problem is whether the map $\Lambda_\sigma \mapsto \sigma$ is continuous. A classic counterexample by Alessandrini [1] demonstrates that stability does not hold in general for a bounded L^∞ conductivity. The counterexample consists of a piecewise constant conductivity in the unit disk with a jump at radius $0 < r < 1$. The DN maps for the conductivity distributions with

and without the jump can be made arbitrarily close in the operator norm by taking $r \rightarrow 0$, but the L^∞ norm of the conductivity difference remains constant. The existence of such a counterexample results from the ill-posedness of the EIT problem.

Conditional stability of the inverse problem can be studied by restricting the domain of the map $\Lambda_\sigma \mapsto \sigma$. In dimension $n > 2$, if σ is required to be in $W^{2,\infty}$, conditional stability holds [1, 2]. In dimension 2, conditional stability was proven for $\sigma \in W^{2,p}$, $p > 1$ in [55], for $\sigma \in C^{1+\alpha}$, $\alpha > 0$ in [10], and $\sigma \in C^\alpha$, $0 < \alpha < 1$ in [11]. Recently, it was shown in [22] that the problem is conditionally stable in the L^p sense for σ uniformly bounded in any fractional Sobolev space $W^{\alpha,p}$ with $\alpha > 0$ and $1 < p < \infty$.

From the practical point of view, conditional stability estimates of the form

$$(1.4) \quad \|\sigma_1 - \sigma_2\|_X \leq Cf(\|\Lambda_{\sigma_1} - \Lambda_{\sigma_2}\|_Y)$$

are unsatisfactory. This is because finite-precision and noisy EIT data is not in general a DN map of any conductivity. A full regularization strategy in the sense of [28, 44] is required instead of (1.4). Recently, the Born approximation in the D-bar method based on [60] was removed and full nonlinear regularization analysis (including estimates on speed of convergence in Banach spaces) given in [50] for twice differentiable conductivities. Providing such regularization analysis for the reconstruction algorithm presented here is an important topic for future work.

For the case of anisotropic conductivities, see [6, 68, 69]. CGO-based solutions can also be used for detecting inclusions in conductivity [18, 38, 37, 39, 40, 71]. For recent development on new kinds of CGO solutions for inverse problems, see [19, 27, 45, 52, 41]. We remark that the assumptions on the boundedness and strict positivity of the conductivity can be relaxed somewhat while retaining uniqueness; on the other hand, losing uniqueness enables invisibility cloaking techniques [34, 35, 54, 30, 31, 32]. The limit of degeneracy of conductivity problem for which the inverse problems is uniquely solvable is studied in [7].

The paper is organized as follows. The CGO solutions are defined in Section 2. The first step in the algorithm is to compute traces of these solutions on $\partial\Omega$ from the Dirichlet-to-Neumann map. The simulation of this map for ideal and noisy data is found in Section 3 and the computation of the traces of the CGO solutions is explained in Section 4.1. The low-pass transport matrix allows us to compute the CGO solutions inside the unit disk from their traces. This step is described in Section 4.2. The reconstruction formula for the conductivity σ is a simple formula given in terms of the CGO solutions inside the unit disk and is also found in Section 4.2. The computational method for solving the Beltrami equations used in the computation of the transport matrix is detailed in Section 5. The results of the numerical tests are found in Section 6. Finally, we conclude our results in Section 7.

2. COMPLEX GEOMETRICAL OPTICS SOLUTIONS

To construct the CGO solutions (1.3), we first define a real-valued function $\mu : \Omega \rightarrow (-1, 1)$ by

$$(2.1) \quad \mu := \frac{1 - \sigma}{1 + \sigma}.$$

We then consider the complex geometrical optics (CGO) solutions $f_\mu = f_\mu(z, k)$ of the Beltrami equation

$$(2.2) \quad \bar{\partial}_z f_\mu = \mu \overline{\partial_z f_\mu},$$

where the solutions can be written in the form

$$(2.3) \quad f_\mu(z, k) = e^{ikz} M_\mu(z, k),$$

and the functions M_μ have the special asymptotics

$$(2.4) \quad M_\mu(z, k) = \left(1 + \mathcal{O}\left(\frac{1}{z}\right) \right) \text{ as } |z| \rightarrow \infty.$$

Here k is a complex parameter. Existence, uniqueness and properties of the CGO solutions are discussed in [4]. Note, however, the key relations for a complex function $f = u + iv$,

$$\bar{\partial}_z f_\mu = \mu \overline{\partial_z f_\mu} \Leftrightarrow \nabla \cdot \sigma \nabla u = 0 \text{ and } \nabla \cdot \sigma^{-1} \nabla v = 0,$$

connecting the PDE's (1.1) and (2.2).

Set

$$(2.5) \quad h_+ = \frac{1}{2}(f_\mu + f_{-\mu}), \quad h_- = \frac{i}{2}(\overline{f_\mu} - \overline{f_{-\mu}}).$$

Then the functions $u_1(z, k)$ and $u_2(z, k)$ in formula (1.3) are given by

$$(2.6) \quad u_1 = h_+ - ih_-, \quad u_2 = i(h_+ + ih_-).$$

An important special feature of the CGO solutions $u_j(z, k)$ is that in the frequency domain they satisfy the equation

$$(2.7) \quad \bar{\partial}_k u_j(z, k) = -i \tau_\sigma(k) \overline{u_j(z, k)}, \quad j = 1, 2,$$

where the coefficient $\tau_\sigma(k)$ does *not* depend on the space variable. For details see [9, Corollary 18.4.4] or [4, Theorem 5.5].

3. SIMULATION OF BOUNDARY DATA

Denote by $\tilde{H}^s(\partial\Omega)$ the space of $H^s(\partial\Omega)$ functions having mean value zero. For arbitrary $g \in \tilde{H}^{-1/2}(\partial\Omega)$, let $u \in H^1(\Omega)$ be the solution of the Neumann problem

$$(3.1) \quad \nabla \cdot \sigma \nabla u = 0 \text{ in } \Omega, \quad \sigma \frac{\partial u}{\partial \nu} = g \text{ on } \partial\Omega.$$

The solution to (3.1) is unique only up to a constant, but the additional requirement $\int_{\partial\Omega} u \, ds = 0$ fixes the solution uniquely. The Neumann-to-Dirichlet (ND) map $\mathcal{R}_\sigma : \tilde{H}^{-1/2}(\partial\Omega) \rightarrow \tilde{H}^{1/2}(\partial\Omega)$ is now defined by $\mathcal{R}_\sigma g = u|_{\partial\Omega}$.

We note two key equalities connecting the DN map Λ_σ and the ND map \mathcal{R}_σ . Define an averaging operator

$$\mathcal{L}\phi := |\partial\Omega|^{-1} \int_{\partial\Omega} \phi \, ds.$$

From the definitions of Λ_σ and \mathcal{R}_σ we see that

$$(3.2) \quad \Lambda_\sigma \mathcal{R}_\sigma = I \quad : \tilde{H}^{-1/2}(\partial\Omega) \rightarrow \tilde{H}^{-1/2}(\partial\Omega),$$

$$(3.3) \quad \mathcal{R}_\sigma \Lambda_\sigma = I - \mathcal{L} \quad : H^{1/2}(\partial\Omega) \rightarrow \tilde{H}^{1/2}(\partial\Omega).$$

In the above we used the fact that for any $f \in H^{1/2}(\partial\Omega)$ we have

$$\mathcal{L}\Lambda_\sigma f = |\partial\Omega|^{-1} \int_{\partial\Omega} \sigma \frac{\partial u}{\partial \nu} \, ds = |\partial\Omega|^{-1} \int_{\Omega} \nabla \cdot \sigma \nabla u = 0.$$

Parameterizing the boundary of our domain by θ , the applied current density $g(\theta)$ must have the property that $\int_0^{2\pi} g(\theta) d\theta = 0$. For $n = 1, \dots, 2N$, define a set of trigonometric basis functions:

$$(3.4) \quad \phi_n(\theta) = \begin{cases} \pi^{-1/2} \cos\left(\frac{(n+1)\theta}{2}\right), & \text{for odd } n, \\ \pi^{-1/2} \sin\left(\frac{n\theta}{2}\right), & \text{for even } n. \end{cases}$$

Any function $g \in L^2(\partial\Omega)$ representing current density on the boundary can then be approximated by

$$(3.5) \quad g(\theta) \approx \sum_{n=1}^{2N} \langle g, \phi_n \rangle \phi_n(\theta),$$

where the inner product is defined for real-valued functions $f, g \in L^2(\partial\Omega)$ by

$$(3.6) \quad \langle f, g \rangle := \int_0^{2\pi} f(\theta)g(\theta) \, d\theta.$$

Given a linear operator $\mathcal{A} : L^2(\partial\Omega) \rightarrow L^2(\partial\Omega)$, define its matrix approximation $A \in \mathbb{R}^{2N \times 2N}$ by setting $A := [A_{mn}]$ with

$$(3.7) \quad A_{mn} := \langle \mathcal{A}\phi_n, \phi_m \rangle.$$

Here $m \in \{1, \dots, 2N\}$ is the row index and $n \in \{1, \dots, 2N\}$ is the column index. Now define the $2N \times 2N$ matrix approximation $[R_{mn}]$ to the ND map by

$$(3.8) \quad R_{mn} = \langle u_n|_{\partial\Omega}, \phi_m \rangle$$

where $u_n|_{\partial\Omega}$ is the solution to (3.1) with $g = \phi_n$.

By equations (3.9) and (4.1) and (4.2) we can approximate \mathcal{H}_μ acting on real-valued, zero-mean functions expanded in the basis (3.4) by

$$(4.3) \quad \tilde{H}_\mu := D_T^{-1} L_\sigma.$$

In general, the traces of the CGO solutions at $\partial\Omega$ do not have mean zero, and so we append the basis function $\phi_0 = (2\pi)^{-1/2}$ to (3.4). This leads to the following $(2N+1) \times (2N+1)$ matrix approximation to the μ -Hilbert transform \mathcal{H}_μ :

$$(4.4) \quad H_\mu := \begin{bmatrix} 0 & 0 \\ 0 & \tilde{H}_\mu \end{bmatrix}.$$

Furthermore, we can approximate $\mathcal{H}_{-\mu}$ when we have H_μ available. We have the identity

$$(4.5) \quad \mathcal{H}_\mu \circ (-\mathcal{H}_{-\mu})u = (-\mathcal{H}_{-\mu}) \circ \mathcal{H}_\mu u = u - \mathcal{L}u,$$

so $-\mathcal{H}_{-\mu}$ is the inverse operator of \mathcal{H}_μ in the subspace of zero-mean functions. Thus we may define a $(2N+1) \times (2N+1)$ matrix approximation to $\mathcal{H}_{-\mu}$:

$$(4.6) \quad H_{-\mu} := \begin{bmatrix} 0 & 0 \\ 0 & -\tilde{H}_\mu^{-1} \end{bmatrix}.$$

Summarizing, once we have measured the DN matrix (3.9), we can approximate the μ -Hilbert transforms $\mathcal{H}_{\pm\mu}$ by matrices $H_{\pm\mu}$ acting on the basis (3.4) augmented by a constant basis function.

However, so far we can only work with *real-valued* functions in $H^{1/2}(\partial\Omega)$, and the CGO solutions are in general complex-valued. Furthermore, the operator \mathcal{H}_μ is not complex-linear but only real-linear: for a real-valued function g we have

$$(4.7) \quad \mathcal{H}_\mu(ig) = i\mathcal{H}_{-\mu}(g).$$

We represent complex-valued functions $g \in H^{1/2}(\partial\Omega)$ by expanding the real and imaginary parts separately and organizing the coefficients as the following vertical vector in \mathbb{R}^{4N+2} :

$$[\langle \operatorname{Re} g, \phi_0 \rangle, \langle \operatorname{Re} g, \phi_1 \rangle, \dots, \langle \operatorname{Re} g, \phi_{2N} \rangle, \langle \operatorname{Im} g, \phi_0 \rangle, \langle \operatorname{Im} g, \phi_1 \rangle, \dots, \langle \operatorname{Im} g, \phi_{2N} \rangle]^T.$$

Now the μ -Hilbert transforms $\mathcal{H}_{\pm\mu}$ can be approximated using the following $(4N+2) \times (4N+2)$ matrices:

$$(4.8) \quad \mathcal{H}_\mu \approx \begin{bmatrix} H_\mu & 0 \\ 0 & H_{-\mu} \end{bmatrix}, \quad \mathcal{H}_{-\mu} \approx \begin{bmatrix} H_{-\mu} & 0 \\ 0 & H_\mu \end{bmatrix},$$

where H_μ and $H_{-\mu}$ are given by (4.4) and (4.6), respectively.

The infinite-precision boundary integral equation is defined as follows. In analogy with the Riesz projections we define the real-linear operator $\mathcal{P}_\mu : H^{1/2}(\partial\mathbb{D}) \rightarrow H^{1/2}(\partial\mathbb{D})$ by the formula

$$(4.9) \quad \mathcal{P}_\mu g = \frac{1}{2}(I + i\mathcal{H}_\mu)g + \frac{1}{2}\mathcal{L}g,$$

where the function g may be complex-valued. Further, denote

$$(4.10) \quad \mathcal{P}_\mu^k := e^{-ikz} \mathcal{P}_\mu e^{ikz},$$

containing complex-linear operators of point-wise multiplication by exponential functions. Matrices for such a multiplication operator (for fixed k) can be constructed quite simply by applying it numerically to each basis function and computing inner products between the result and each basis function.

It was shown in [5] that the following boundary integral equation holds:

$$(4.11) \quad M_\mu(\cdot, k)|_{\partial\mathbb{D}} + 1 = (\mathcal{P}_\mu^k + \mathcal{P}_0)M_\mu(\cdot, k)|_{\partial\mathbb{D}},$$

where the function M_μ is as in (2.3). We can thus solve (4.11) for the trace of $M_\mu(\cdot, k)$ on $\partial\Omega$ and use (2.3) to find the trace of $f_\mu(\cdot, k)$ as well.

Numerical solution of (4.11) is done by writing real and imaginary parts separately, replacing all the operators by their $(4N+2) \times (4N+2)$ matrix approximations, and solving the resulting finite linear system in a regularized manner.

Because of the conjugation with exponential functions in (4.10), the error in H_μ gets multiplied with numbers exponentially large in k , and so we can only reliably numerically solve the boundary integral equation (4.11) for k ranging in a disc $D(0, R)$ where the radius $R > 0$ depends on the noise level. This is where the exponential ill-posedness of the inverse conductivity problem shows up in our reconstruction method. We regularize the reconstruction by truncation of coefficient functions to the disc $|k| < R$; in other words replacing the function values by zero outside that disc.

4.2. The low-pass transport matrix and conductivity reconstruction.

Suppose we know the trace of the CGO solution $f_\mu(\cdot, k)$ on $\partial\Omega$. Then we can expand it as a Fourier series at the boundary. Now equation (2.2) and the fact that μ is supported in Ω implies that $f_\mu(\cdot, k)$ is analytic outside the unit disc. Therefore the coefficients of the Fourier series can be used to expand f_μ as a power series outside Ω . In other words, the trace of $f_\mu(\cdot, k)$ on $\partial\Omega$ determines f_μ outside Ω in a straightforward way.

Choose then a point $z_0 \in \mathbb{R}^2 \setminus \overline{\Omega}$. As explained above, we know $f_\mu(z_0, k)$ and $f_{-\mu}(z_0, k)$ for any $|k| < R$. Use (2.5) to construct the function

$$(4.12) \quad \nu_{z_0}^{(R)}(k) := \begin{cases} i \frac{h_-(z_0, k)}{h_+(z_0, k)} & \text{for } |k| < R, \\ 0 & \text{for } |k| \geq R. \end{cases}$$

We next solve the truncated Beltrami equations

$$(4.13) \quad \bar{\partial}_k \alpha^{(R)} = \nu_{z_0}^{(R)}(k) \overline{\partial_k \alpha^{(R)}},$$

$$(4.14) \quad \bar{\partial}_k \beta^{(R)} = \nu_{z_0}^{(R)}(k) \overline{\partial_k \beta^{(R)}},$$

with solutions represented in the form

$$(4.15) \quad \alpha^{(R)}(z, z_0, k) = \exp(ik(z - z_0) + \varepsilon(k)),$$

$$(4.16) \quad \beta^{(R)}(z, z_0, k) = i \exp(ik(z - z_0) + \tilde{\varepsilon}(k)),$$

where $\varepsilon(k)/k \rightarrow 0$ and $\tilde{\varepsilon}(k)/k \rightarrow 0$ as $k \rightarrow \infty$. Requiring

$$(4.17) \quad \alpha^{(R)}(z, z_0, 0) = 1 \quad \text{and} \quad \beta^{(R)}(z, z_0, 0) = i$$

fixes the solutions uniquely, see Section 5.1.

Fix any nonzero $k_0 \in \mathbb{C}$ and choose any point z inside the unit disc. We can now use the approximate transport matrix

$$(4.18) \quad T^{(R)} = T_{z, z_0, k_0}^{(R)} := \begin{pmatrix} a_1^{(R)} & a_2^{(R)} \\ b_1^{(R)} & b_2^{(R)} \end{pmatrix}$$

to compute

$$(4.19) \quad \begin{aligned} u_1^{(R)}(z, k_0) &= a_1^{(R)} u_1(z_0, k_0) + a_2^{(R)} u_2(z_0, k_0), \\ u_2^{(R)}(z, k_0) &= b_1^{(R)} u_1(z_0, k_0) + b_2^{(R)} u_2(z_0, k_0), \end{aligned}$$

where $\alpha^{(R)} = a_1^{(R)} + ia_2^{(R)}$ and $\beta^{(R)} = b_1^{(R)} + ib_2^{(R)}$. The truncation in (4.12) can be interpreted as a nonlinear low-pass filter in the k -plane. This is where the term *low-pass transport matrix* originates.

To see the role of equations (4.19) recall that since $u_1(z_0, k_0)$ and $u_2(z_0, k_0)$ are \mathbb{R} -linearly independent [9, Theorem 18.4.1], we can always write $u_j(z, k_0)$ as a linear combination of them. However, the key point here is that, e.g. if we write $u_1(z, k_0) = a_1 u_1(z_0, k_0) + a_2 u_2(z_0, k_0)$, then a straightforward calculation using the $\bar{\partial}_k$ -equations (2.7) implies that the function $\alpha = a_1 + ia_2$ satisfies equation (4.13) with the untruncated coefficient $\nu_{z_0}(k)$. Furthermore (4.15) holds with $\alpha(z, z_0, 0) = 1$, see [4], and similar argument applies to $\beta(z, z_0, k)$.

Given the above we know the approximate solutions $u_j^{(R)}(z, k_0)$ for $z \in \mathbb{D}$ and one fixed k_0 . We use formulas (2.5) and (2.6) to connect $u_1^{(R)}, u_2^{(R)}$ with $f_\mu^{(R)}, f_{-\mu}^{(R)}$. Define

$$(4.20) \quad \mu^{(R)}(z) = \frac{\bar{\partial} f_\mu^{(R)}(z, k_0)}{\partial f_\mu^{(R)}(z, k_0)}.$$

Finally we reconstruct the conductivity σ approximatively as

$$(4.21) \quad \sigma^{(R)} = \frac{1 - \mu^{(R)}}{1 + \mu^{(R)}}.$$

Note that the limit $R \rightarrow \infty$ corresponds to the perfect reconstruction from infinite-precision data described in [4].

5. BELTRAMI EQUATION SOLVER

We now show that the problems (4.13)-(4.16) have unique solutions given the requirement that the transport matrix be the identity at $k = 0$. With the truncation of ν_{z_0} to $\nu_{z_0}^{(R)}$ the sublinear terms $\varepsilon(k)$ and $\tilde{\varepsilon}(k)$ in (4.15)-(4.16) become analytic outside the disk of radius R (apply here [9, Theorem 5.5.1]), hence bounded and this in turn results in \mathbb{R} -linear equations for which numerical solvers were studied in [8, 36].

Below, we keep the variable z fixed.

5.1. Constructing the low-pass transport matrix. Assume $2 < p < 1 + 1/q$, where q is a constant such that $|\nu_{z_0}^{(R)}(k)| \leq q < 1$ for all $k \in \mathbb{C}$ [4, Proposition 6.3]. To construct the truncated transport matrix (4.18), first find solutions $\eta_1, \eta_2 \in W_{\text{loc}}^{1,p}(\mathbb{R}^2)$ to the equation

$$(5.1) \quad \bar{\partial}_k \eta = \nu_{z_0}^{(R)}(k) \overline{\partial_k \eta},$$

with asymptotics

$$(5.2) \quad \eta_1(k) = e^{ik(z-z_0)}(1 + \mathcal{O}(1/z)) \quad \text{and} \quad \eta_2(k) = i e^{ik(z-z_0)}(1 + \mathcal{O}(1/z)),$$

respectively, as $|k| \rightarrow \infty$. Such solutions exist and are unique by [4, Theorem 4.2]. In fact, we are here constructing CGO solutions, but now in the frequency domain.

The solutions are complex valued, but pointwise \mathbb{R} -linearly independent by [9, Theorem 18.4.1]. Hence there are constants $A, B \in \mathbb{R}$ such that

$$A \eta_1(0) + B \eta_2(0) = 1.$$

We now set

$$\alpha^{(R)}(z, z_0, k) = A \eta_1(k) + B \eta_2(k), \quad k \in \mathbb{R}^2.$$

Then $\alpha^{(R)}(z, z_0, k)$ satisfies (4.13) and the first condition in (4.17). Applying [4, Corollary 3.4] to $F(k) := e^{-ik(z-z_0)} \alpha^{(R)}(z, z_0, k)$ gives

$$F(k) = \exp(C_0 + \varepsilon(k)), \quad C_0 \text{ a constant and } \varepsilon(k) \rightarrow 0 \text{ as } k \rightarrow \infty.$$

Thus we have the required asymptotics (4.15), completing the construction of $\alpha^{(R)}(z, z_0, k)$. Applying similarly [4, Corollary 3.4] to the difference of two solutions to (4.13), (4.15) shows that if the solutions agree at one point, then they are identical. Hence we have also the uniqueness of the function $\alpha^{(R)}(z, z_0, k)$. The same argument with [4, Corollary 3.4] also shows that at every k , the function values $\alpha^{(R)}(z, z_0, k), \beta^{(R)}(z, z_0, k)$ are \mathbb{R} -linearly independent. Thus the low-pass transport matrices are invertible at every point.

5.2. Solving \mathbb{R} -linear Beltrami equations. To solve the equation (5.1) with either of the asymptotics in (5.2) we argue as in [4]. Making the substitution $\eta(k) = e^{ik(z-z_0)}(1 + \omega(k))$ we obtain the \mathbb{R} -linear equation

$$(5.3) \quad \bar{\partial}_k \omega + \gamma_1 \overline{\partial_k \omega} + \gamma_2 \bar{\omega} + \gamma_2 = 0$$

with the asymptotic condition $\lim_{k \rightarrow \infty} \omega(k) = 0$, where

$$(5.4) \quad \gamma_1(z, z_0, k) = \pm e_{-(z-z_0)}(k) \nu_{z_0}^{(R)}(k),$$

$$(5.5) \quad \gamma_2(z, z_0, k) = -i \overline{(z - z_0)} \gamma_1(z, z_0, k),$$

with $e_z(k) = e^{i(kz + \bar{k}\bar{z})}$. We solve numerically this equation as described in [36].

Substitute $u \in L^p(D(0, R))$ such that $\bar{u} = -\bar{\partial}_k \omega$. Then $\omega = -P\bar{u}$ and $\partial_k \omega = -S\bar{u}$, where P is the solid Cauchy transform and S is the Beurling transform defined by

$$Pf(z) = -\frac{1}{\pi} \int_{\mathbb{C}} \frac{f(\lambda)}{\lambda - z} dm(\lambda), \quad Sg(z) = -\frac{1}{\pi} \int_{\mathbb{C}} \frac{g(\lambda)}{(\lambda - z)^2} dm(\lambda),$$

where the latter is a principal value integral, the points $(\lambda_1, \lambda_2) \in \mathbb{R}^2$ and $\lambda_1 + i\lambda_2 \in \mathbb{C}$ are identified, and dm denotes Lebesgue measure in \mathbb{R}^2 . This leads to the \mathbb{R} -linear integral equation

$$(5.6) \quad u + (\overline{\gamma_1} S + \overline{\gamma_2} P)\bar{u} = \overline{\gamma_2}.$$

5.3. Discretization. We form a uniform grid in $[-R, R]^2$ allowing the use of fast Fourier transform (FFT) for matrix-vector products. Choose a positive integer m , let $N = 2^m$, $h = 2R/N$ and define

$$(5.7) \quad \mathbb{Z}_N^2 = \{(j_1, j_2) \in \mathbb{Z}^2 \mid -N/2 \leq j_1, j_2 < N/2\}.$$

The uniform grid consists of the points $\{jh \mid j \in \mathbb{Z}_N^2\}$.

The grid approximation of a function $v : [-R, R]^2 \rightarrow \mathbb{C}$ is defined by $v_h : \mathbb{Z}_N^2 \rightarrow \mathbb{C}$ with $v_h(j) := v(jh)$. The Cauchy transform Pv and the Beurling transform Sv are discretized by

$$(P_h v_h)(j) = \frac{1}{\pi h} \sum_{\substack{l \neq j \\ l \in \mathbb{Z}_N^2}} \frac{1}{j - l} v_h(l), \quad (S_h v_h)(j) = -\frac{1}{\pi} \sum_{\substack{l \neq j \\ l \in \mathbb{Z}_N^2}} \frac{1}{(j - l)^2} v_h(l),$$

where $(Pv)(jh) \approx (P_h v_h)(j)$ and $(Sv)(jh) \approx (S_h v_h)(j)$ for $j \in \mathbb{Z}_N^2$. The Toeplitz structure of these discretizations allows fast computation of the products $P_h v_h$ and $S_h v_h$ by executing the FFT.

The functions γ_i ($i = 1, 2$) are discretized by

$$\gamma_{i,h}(j) = \gamma_i(z, z_0, jh).$$

Finally, we obtain the discretized form of (5.6) as

$$(5.8) \quad u_h + (\overline{\gamma_{1,h}} S_h + \overline{\gamma_{2,h}} P_h)\bar{u}_h = \overline{\gamma_{2,h}}$$

and $\omega_h = -P_h \overline{w_h}$ is an approximate solution to (5.3). To solve this equation, we execute the iterative generalized minimal residual (GMRES) method [63] by using a preconditioner we describe next.

We make a substitution to (5.8) having a two-fold advantage. Let $A_h = \overline{\gamma_{1,h}} S_h + \overline{\gamma_{2,h}} P_h$ and substitute $u_h = w_h - A_h \overline{w_h}$. We then get a \mathbb{C} -linear equation

$$(5.9) \quad (I - A_h \overline{A_h}) w_h = \overline{\gamma_{2,h}},$$

where $\overline{A_h} w_h = \overline{A_h \overline{w_h}}$. This preconditioning resulted in the fastest convergence of GMRES for the equation (5.8) in comparison to the other options considered in [36].

The second advantage of this substitution comes from the requirement of having to solve two Beltrami equations of type (5.3) for each z -point as described in Section 5.1. Let us denote the functions and operators corresponding to the first equation by $\gamma_{i,h}^+$ ($i = 1, 2$) and A_h^+ , and those of the second equation by $\gamma_{i,h}^-$ and A_h^- . We notice that $\gamma_i^- = -\gamma_i^+$. Therefore $A_h^- = -A_h^+$ as well, resulting in $I - A_h^+ \overline{A_h^+} = I - A_h^- \overline{A_h^-}$. Hence, to solve the two equations

$$\begin{aligned} (I - A_h^+ \overline{A_h^+}) w_h^+ &= \overline{\gamma_{2,h}^+}, \\ (I - A_h^- \overline{A_h^-}) w_h^- &= \overline{\gamma_{2,h}^-} \end{aligned}$$

we merely solve the first one and then set $w_h^- = -w_h^+$.

6. NUMERICAL RESULTS

Four example conductivities are studied: a simple heart-and-lungs phantom σ_1 related to monitoring intensive care patients, similar heart-and-lungs phantoms σ_2 and σ_3 both featuring a low-conductivity spine, and σ_2 an additional tumor-like inhomogeneity inside one of the lungs. The fourth example is a conductivity cross-section σ_4 of a stratified medium that could arise, for example, in an oil pipeline or other industrial process monitoring applications.

All these conductivities are discontinuous and therefore violate the assumptions of previously published D-bar reconstruction methods.

6.1. Heart-and-lungs phantom. We define an idealized computational model of a cross-section of a patient's chest, see the leftmost image in Figure 2. The conductivity values are

| | |
|-------------|------|
| Background | 1.0, |
| Lung (blue) | 0.7, |
| Heart (red) | 2.0. |

We simulate boundary measurements using FEM to solve equation (3.1). We let n range from 1 to 32, so $N = 16$. This choice corresponds approximately to an EIT configuration with 32 equispaced electrodes located on the unit circle. Our FEM mesh comprises 263 169 nodes and 524 288 triangles. According to a numerical test comparing analytically and numerically computed ND maps for

the constant conductivity $\sigma \equiv 1$, our computed ND matrix elements have at least 5 correct digits. This accuracy is achievable in practice; for instance, the 32-electrode ACT3 system of Rensselaer Polytechnic Institute is actually capable of somewhat higher accuracy [23]. Also, we construct data with 0.01% noise using (3.9).

We solve the matrix version of the boundary integral equation (4.11) for the traces of CGO solutions with k ranging in a finite grid inside the disc $|k| < R$. Regularization is implemented using the Moore-Penrose pseudoinverse. The cutoff frequency R is taken as large as possible without too much numerical error, resulting in $R = 6$ for the data with no added noise and $R = 5.5$ for the data with 0.01% noise. More advanced or automatic choices of R are not discussed in this work.

We choose $z_0 = 1.4$ and use (4.12) to evaluate the function $\nu_{z_0}^{(R)}(k)$ numerically in the disc $|k| < R$. Plot of ν_{z_0} with $R = 6$ is shown in Figure 1. Further, we choose the point k_0 in Section 4.2 as the nearest k -grid point to 1.

We construct a finite Cartesian grid of points in the unit disc, and for each of those points $z \in \Omega$ the truncated Beltrami equation (4.13) for $\alpha^{(R)}$ is solved using the quasilinear asymptotic condition (4.15) depending on z . Substituting the result into (4.20) and (4.21) yields an approximate reconstruction of the conductivity at z . Numerical differentiation in (4.20) is not problematic as the low-pass filtering results in smooth functions to be differentiated.

Figure 2 shows the two reconstructions together with relative errors given by

$$(6.1) \quad \frac{\|\sigma - \sigma^{(R)}\|_{L^2(\Omega)}}{\|\sigma\|_{L^2(\Omega)}} \cdot 100\%.$$

The relative errors of the reconstructions are 11.6% and 12.7%.

Further, we define the dynamic range of a reconstruction to be 100% multiplied by the ratio of the difference of the maximum and minimum values in the reconstruction to the difference of maximum and minimum values of the true conductivity. The minimum conductivity in the noise-free reconstruction is 0.637 (compared to a true value of 0.7), and the maximum conductivity is 1.997 (compared to a true value of 2). This results in a dynamic range of 105%. The minimum conductivity in the reconstruction from data with 0.01% noise is 0.637 and the maximum 1.870, resulting in a dynamic range of 95%.

The reconstructions display a high degree of spatial accuracy and lack of artifacts. Notably, the separation between the lungs is clearly visible and the organs are not distorted toward the boundary of the domain.

We remark that different choices for z_0 and k_0 result in slightly differing numerical values in the reconstruction, but we do not discuss such effects further here (with the exception of using several z_0 values in Subsection 6.3).

6.2. Heart-and-lungs phantom with tumor. We define another model σ_2 of a cross-section of a patient's chest but now with a resistive spine and a conductive

“tumor” in the right lung. The conductivity σ_3 is the same as σ_2 but without the tumor, see Figure 3. The conductivity values are

| | |
|-------------------|------|
| Background | 1.0, |
| Lung (light blue) | 0.7, |
| Spine (dark blue) | 0.2, |
| Heart (red) | 2.0, |
| Tumor (red) | 2.0. |

We compute reconstructions from data with no added noise using $R = 5.5$ and otherwise the same parameters as in Subsection 6.1, see Figure 3. Relative errors in the reconstructions of σ_2 and σ_3 are 16.7% and 16.3% and the dynamic ranges are 109% and 106%, respectively. The latter are computed using the differences between the heart and spine since the maximum and minimum conductivity values occur there.

While the heart, lungs, and spine are all clearly visible, the spine appears somewhat enlarged in the reconstructions, and the separation between the lungs and spine is not as marked as the separation between other organs.

The conductivity of the tumor is 2, the same as that of the heart. However, while the presence of the tumor is evident in the reconstructed image as a region of brighter blue in the lung, its actual conductivity value is not well-reconstructed. A difference image is also included in Figure 3 in which the reconstruction without the tumor is subtracted from the reconstruction with the tumor. In the difference image, the tumor is strikingly visible, but we note that it is plotted on its own scale, not relative to the plots above. The true contrast in the difference image is 1.3, while the contrast achieved in the difference image is 0.2073.

6.3. Stratified medium. The conductivity σ_4 consists of horizontal layers as shown in the bottom left image in Figure 4. The conductivity values are

| | |
|--------------|------|
| Top layer | 1.2, |
| Middle layer | 2.0, |
| Bottom layer | 0.3. |

Such a conductivity could be a rough model of a cross-section of an oil pipeline with sand in the bottom, water in the middle, and oil on top.

Unlike the previous examples, the conductivity σ_4 is not constant near the boundary. This violates the assumptions of the proposed method, and we take this into account as follows. The cross-section of the pipeline is modeled by the disc $|x| \leq 0.7$, and we define $\sigma_3(x) \equiv 1$ for $0.7 < |x| \leq 1$. In principle one could measure EIT data at the boundary $|x| = 0.7$ of the pipeline and determine the DN map on $|x| = 1$ as explained for infinite-precision data in [60, Section 6] and numerically implemented for noisy data in [66]. However, we take the simpler approach of adding the layer around the boundary $0.7 < |x| \leq 1$ in which $\sigma_3 = 1$ and simulating the DN map on $|x| = 1$.

We compute the function ν_{z_0} with $R = 4$ and $z_0 = 1.4$, see Figure 1. The truncation radius is determined visually by increasing it as far as possible before apparent numerical instability. We observe a nonsymmetry in the reconstruction, the highest quality being at the points closest to $z_0 = 1.4$. To obtain a more symmetric reconstruction, we compute four reconstructions $\sigma_E, \sigma_W, \sigma_N, \sigma_S$ computed using $z_0 = 1.4, -1.4, 1.4i, -1.4i$, respectively. Figure 4 shows the combined reconstruction defined by

$$(6.2) \quad \sigma = .25(1 + z_1)\sigma_E + .25(1 - z_1)\sigma_W + .25(1 + z_2)\sigma_N + .25(1 - z_2)\sigma_S.$$

The idea of the weighted sum (6.2) is to emphasize the highest-quality parts of each of the four reconstructions.

The layers are very clearly represented with very few artifacts. One observable artifact is the smoothing that occurs between the layers. However the gradient is quite steep and so it is readily recognized as a layer. The relative error is 24.7% and the dynamic range is 134% inside the disc $|x| < 0.7$.

7. DISCUSSION AND SUMMARY

In this work a new computational EIT algorithm in dimension two is presented, based on the constructive uniqueness proof given by Astala and Päivärinta in [*Ann. of Math.* **163** (2006)]. The method consists of three main steps. First, one must recover traces of CGO solutions from the DN map by solving an ill-posed boundary integral equation introduced in [5]. Second, one approximates the CGO solutions inside the unit disc using a *low-pass transport matrix*. Finally, the approximate conductivity is computed from the CGO solutions inside the unit disc using numerical differentiation and simple algebra.

A fast solver of the Beltrami equation, introduced in [36], was employed to facilitate the computation of the low-pass transport matrix. We stress that although the Beltrami solver is based on the iterative GMRES algorithm, the proposed EIT reconstruction method involves no iterations in the conductivity space.

The method was tested on simulated conductivity distributions with applications in medical imaging and process tomography. The results were very robust with respect to noise in the data and gave a very good representation of the dynamic range of the actual conductivity distribution. The reconstructions are mollified approximations to the discontinuous conductivities, but the gradients are quite steep. Relative errors in the reconstructions are of the same size (or slightly smaller) than similar errors for previous D-bar methods assuming smoothness in the conductivity.

The excellent dynamic range and good spatial resolution indicate that this method holds promise for applications and use with experimental data.

ACKNOWLEDGEMENTS

This material is based upon work supported by the Finnish Centre of Excellence in Inverse Problems Research (Academy of Finland CoE-project 213476, L. Päivärinta and S. Siltanen) and by the Finnish Center of Excellence in Analysis and Dynamics Research (Academy of Finland projects 1118634 and 118422, K. Astala). The work of S. Siltanen was supported in part by the Computational Science Research Programme of the Academy of Finland (project 134868).

REFERENCES

- [1] G. Alessandrini, Stable determination of conductivity by boundary measurements, *Appl. Anal.* **27** (1988), 153–172.
- [2] G. Alessandrini, Singular solutions of elliptic equations and the determination of conductivity by boundary measurements, *J. Diff. Eq.* **84** (1990), 252–272.
- [3] G. Alessandrini and E. Cabib, EIT and average conductivity, *J. Inv. Ill-Posed Problems* **15** (2005), 207–241.
- [4] K. Astala and L. Päivärinta, Calderón’s inverse conductivity problem in the plane, *Ann. of Math.* **163** (2006), 265–299.
- [5] K. Astala and L. Päivärinta, *A boundary integral equation for Calderón’s inverse conductivity problem*, Proc. 7th Internat. Conference on Harmonic Analysis, Collectanea Mathematica, 2006
- [6] K. Astala, M. Lassas and L. Päivärinta, Calderón’s inverse problem for anisotropic conductivity in the plane, *Comm. Partial Differential Equations* **30** (2005), 207–224.
- [7] K. Astala, M. Lassas, and L. Päivärinta, Limits of visibility and invisibility for Calderón’s inverse problem in the plane, in preparation.
- [8] Astala K, Mueller J L, Paivarinta L and Siltanen S, *Numerical computation of complex geometrical optics solutions to the conductivity equation*. To appear in Applied and Computational Harmonic Analysis.
- [9] K. Astala, T. Iwaniec and G. Martin, Elliptic Partial Differential Equations and Quasiconformal Mappings in the Plane, *Princeton University Press, Princeton, NJ, 2009*.
- [10] J. A. Barceló, T. Barceló and A. Ruiz, Stability of the Inverse Conductivity Problem in the Plane for Less Regular Conductivities, *J. Differential Equations* **173** (2001), 231–270.
- [11] T. Barceló and D. Faraco and A. Ruiz Stability of Calderón inverse conductivity problem in the plane *J. Math. Pures Appl.* **88** (2007), 522–556.
- [12] J. Bikowski Electrical Impedance Tomography Reconstructions in Two and Three Dimensions; from Calderón to Direct Methods *PhD thesis, Colorado State University, Fort Collins, CO, (2008)*.
- [13] J. Bikowski and J. L. Mueller 2D EIT reconstructions using Calderon’s method *Inverse Problems and Imaging* **2** (2008), 43–61.
- [14] J. Bikowski, K. Knudsen, J. L. Mueller, Direct numerical reconstruction of conductivities in three dimensions. arXiv:1003.3764v1
- [15] Boverman G, Isaacson D, Kao T-J, Saulnier G J and Newell J C 2008 Methods for Direct Image Reconstruction for EIT in Two and Three Dimensions *Proceedings of the 2008 Electrical Impedance Tomography Conference took place at Dartmouth College, in Hanover, New Hampshire, USA, June 16 to 18, 2008*
- [16] R. Brown and R. Torres, Uniqueness in the inverse conductivity problem for conductivities with $3/2$ derivatives in L^p , $p > 2n$, *J. Fourier Analysis Appl.*, **9** (2003), 1049–1056.

- [17] R. M. Brown and G. Uhlmann, *Uniqueness in the inverse conductivity problem for non-smooth conductivities in two dimensions*, *Comm. Partial Differential Equations* **22**, 1009 (1997).
- [18] M. Brühl and M. Hanke, Numerical implementation of two non-iterative methods for locating inclusions by impedance tomography, *Inverse Problems* **16** (2000), 1029
- [19] A. Bukhgeim, Recovering the potential from Cauchy data in two dimensions, *J. Inverse Ill-Posed Probl.*, **16** (2008), 19–34.
- [20] A. P. Calderón, *On an inverse boundary value problem*, In seminar on numerical analysis and its applications to continuum physics, Soc. Brasileira de Matemática, (1980), pp. 65–73.
- [21] M. Cheney, D. Isaacson and J. C. Newell, *Electrical Impedance Tomography*, *SIAM Review* **41** (1999), pp. 85–101.
- [22] A. Clop, D. Faraco and A. Ruiz, Integral stability of Calderón inverse conductivity problem in the plane. arXiv:0807.4148.
- [23] Cook R D, Saulnier G J and Goble J C 1991, *A phase sensitive voltmeter for a high-speed, high-precision electrical impedance tomograph* in Proc. Annu. Int. Conf. IEEE Engineering in Medicine and Biology Soc., 1991, pp. 22–23.
- [24] H. Cornean, K. Knudsen, and S. Siltanen. Towards a D-bar reconstruction method for three-dimensional EIT. *Journal of Inverse and Ill-posed Problems* **12** (2006), 111–134.
- [25] P. Daripa, *A fast algorithm to solve the Beltrami equation with applications to quasiconformal mappings*, *Journal of Computational Physics*, **106** (1993), pp. 355–365.
- [26] M. DeAngelo and J. L. Mueller. D-bar reconstructions of human chest and tank data using an improved approximation to the scattering transform, *Physiological Measurement* **31** (2010), 221–232.
- [27] D. Dos Santos Ferreira, C. Kenig, J. Sjöstrand and G. Uhlmann, Determining the Magnetic Schrödinger Operator from Partial Cauchy Data. *Comm. Math. Phys.* **271** (2007), 467–488.
- [28] H. Engl, M. Hanke and A. Neubauer, *Regularization of Inverse Problems*, *Springer* (2000).
- [29] D. Gaydashev and D. Khmelev, *On numerical algorithms for the solution of a Beltrami equation*, arXiv:math.NA/0510516 (2005)
- [30] A. Greenleaf, Y. Kurylev, M. Lassas, G. Uhlmann: Full-wave invisibility of active devices at all frequencies, *Comm. Math. Phys.* **275** (2007), 749–789.
- [31] A. Greenleaf, Y. Kurylev, M. Lassas, G. Uhlmann, Cloaking Devices, Electromagnetic Wormholes and Transformation Optics. To appear in *SIAM Review*.
- [32] A. Greenleaf, M. Lassas, and G. Uhlmann, Invisibility and inverse problems *Bull. Amer. Math. Soc.* **46** (2009), 55–97.
- [33] A. Greenleaf, M. Lassas, and G. Uhlmann, The Calderón problem for conormal potentials, I: Global uniqueness and reconstruction, *Comm. Pure Appl. Math* **56** (2003), 328–352.
- [34] A. Greenleaf, M. Lassas, and G. Uhlmann, Anisotropic conductivities that cannot be detected in EIT, *Physiol. Meas.* (special issue on Impedance Tomography), **24** (2003), 413–420.
- [35] A. Greenleaf, M. Lassas, and G. Uhlmann, On nonuniqueness for Calderón’s inverse problem, *Math. Res. Lett.* **10**, 5–6, (2003), 685–693.
- [36] M. Huhtanen and A. Perämäki, *Numerical solution of the \mathbb{R} -linear Beltrami equation*, submitted manuscript.
- [37] Ide T, Isozaki H, Nakata S and Siltanen S 2010, Local detection of three-dimensional inclusions in electrical impedance tomography. *Inverse Problems* **26** 035001.
- [38] T. Ide, H. Isozaki, S. Nakata, S. Siltanen, and G. Uhlmann, Probing for electrical inclusions with complex spherical waves. *Communications on Pure and Applied Mathematics* **60** (2007), 1415–1442.
- [39] M. Ikehata and S. Siltanen, Numerical method for finding the convex hull of an inclusion in conductivity from boundary measurements, *Inverse Problems* **16** (2000), 1043–1052.

- [40] M. Ikehata and S. Siltanen, Electrical impedance tomography and Mittag-Leffler's function, *Inverse Problems* **20** (2004), 1325–1348.
- [41] O. Y. Imanuvilov, G. Uhlmann, and M. Yamamoto, The Calderón problem with partial data in two dimensions, *J. Amer. Math. Soc.* **23** (2010), 655–691.
- [42] D. Isaacson, J. L. Mueller, J. C. Newell, and S. Siltanen. *Reconstructions of chest phantoms by the D-bar method for electrical impedance tomography*, *IEEE Trans. Med. Im.* **23** (2004) pp. 821–828.
- [43] D. Isaacson, J. L. Mueller, J. C. Newell, and S. Siltanen, Imaging cardiac activity by the D-bar method for electrical impedance tomography, *Physiological Measurement* **27** (2006), S43–S50
- [44] B. Kaltenbacher, A. Neubauer and O. Schertzer, Iterative Regularization Methods for Nonlinear Ill-posed Problems, Walter de Gruyter & Co 2008.
- [45] C.E. Kenig, J. Sjöstrand and G. Uhlmann, The Calderón problem with partial data, *Annals of Math.* **165** (2007), 567–591.
- [46] K. Knudsen, On the Inverse Conductivity Problem, *Ph.D. thesis*, Department of Mathematical Sciences, Aalborg University, Denmark (2002)
- [47] K. Knudsen, A new direct method for reconstructing isotropic conductivities in the plane, *Physiol. Meas.* **24** (2003), 391–401.
- [48] K. Knudsen, M. Lassas, J. L. Mueller and S. Siltanen, Reconstructions of piecewise constant conductivities by the D-bar method for electrical impedance tomography, *Proceedings of Applied Inverse Problems 2007, Vancouver*, in press.
- [49] K. Knudsen, M. Lassas, J. L. Mueller and S. Siltanen, D-bar method for electrical impedance tomography with discontinuous conductivities, *SIAM J. Appl. Math.* **67** (2007), 893–913.
- [50] Knudsen K, Lassas M, Mueller J L and Siltanen S 2009, Regularized D-bar method for the inverse conductivity problem. *Inverse Problems and Imaging* **3**(4), pp. 599-624.
- [51] K. Knudsen, J. L. Mueller and S. Siltanen. *Numerical solution method for the dbar-equation in the plane*. *J. Comp. Phys.* **198** (2004) pp. 500–517.
- [52] K. Knudsen and M. Salo, Determining nonsmooth first order terms from partial boundary measurements, *Inverse Problems and Imaging* **1** (2007), 349–369
- [53] K. Knudsen and A. Tamasan, *Reconstruction of less regular conductivities in the plane*, *Comm. Partial Differential Equations* **29** (2004) pp. 361–381
- [54] M. Lassas, M. Taylor, and G. Uhlmann, The Dirichlet-to-Neumann map for complete Riemannian manifolds with boundary, *Comm. Geom. Anal.* **11** (2003), 207–222.
- [55] L. Liu, Stability Estimates for the Two-Dimensional Inverse Conductivity Problem, *Ph.D. thesis*, University of Rochester, 1997.
- [56] J. L. Mueller and S. Siltanen. *Direct reconstructions of conductivities from boundary measurements*. *SIAM J. Sci. Comp.*, **24** (2003) pp.1232–1266.
- [57] J. L. Mueller, S. Siltanen, and D. Isaacson. A direct reconstruction algorithm for electrical impedance tomography. *IEEE Trans. Med. Im.* **21** **6**, (2002), 555–559.
- [58] E. Murphy, J. L. Mueller, and J. C. Newell. Reconstruction of conductive and insulating targets using the D-bar method on an elliptical domain. *Physiol. Meas.* **28** (2007), S101–S114.
- [59] A. I. Nachman. Reconstructions from boundary measurements. *Ann. of Math.* **128** (1988), 531–576.
- [60] A. I. Nachman, *Global uniqueness for a two dimensional inverse boundary value problem*, *Ann. of Math.* **143** (1996), pp. 71–96.
- [61] R. G. Novikov A multidimensional inverse spectral problem for the equation $-\Delta\psi+(v(x)-Eu(x))\psi=0$, *Funktsional. Anal. i Prilozhen.* **22** 11–22 (transl.) *Funct. Anal. Appl.* **22** (1988), 263–272.

- [62] L. Päivärinta, A. Panchenko, and G. Uhlmann, Complex geometrical optics for Lipschitz conductivities, *Rev. Mat. Iberoam.* **19** (2003), 57–72.
- [63] Y. Saad and M. H. Schultz, GMRES: A generalized minimal residual algorithm for solving nonsymmetric linear systems, *SIAM J. Sci. Stat. Comput.* **7** (1986), 856–869.
- [64] S. Siltanen, J. Mueller and D. Isaacson *An implementation of the reconstruction algorithm of A. Nachman for the 2-D inverse conductivity problem*, *Inverse Problems* 16 (2000), pp.681-699 (Erratum: *Inverse problems* **17**, 1561–1563)
- [65] S. Siltanen, J. Mueller, and D. Isaacson Reconstruction of High Contrast 2-D Conductivities by the Algorithm of A. Nachman., In *AMS proceedings of the 2000 conference on Radon Transforms and Tomography*, Contemporary Mathematics 278, (2001), E. Quinto, editor, 241–254.
- [66] Siltanen S and Tamminen J, Reconstructing conductivities with boundary corrected D-bar method. Submitted manuscript.
- [67] G. Strang and G. Fix: *An Analysis of The Finite Element Method*. Prentice Hall (1973).
- [68] Z. Sun and G. Uhlmann, Anisotropic inverse problems in two dimensions, *Inverse Problems* **19** (2003), 1001–1010.
- [69] J. Sylvester, An anisotropic inverse boundary value problem, *Comm. Pure Appl. Math.* **43** (1990), 201–232.
- [70] J. Sylvester and G. Uhlmann, *A global uniqueness for an inverse boundary value problem*, *Ann. of Math.* 125 (1987), pp. 153–169.
- [71] G. Uhlmann and J-N. Wang, Complex geometrical optics solutions and reconstruction of discontinuities *SIAM J. Appl. Math.* **68** (2008), 1026–1044.
- [72] G. Vainikko, Fast solvers of the Lippmann–Schwinger equation, in *Direct and Inverse Problems of Mathematical Physics* (Newark, DE), Kluwer Acad. Publ, Dordrecht, Int. Soc. Anal. Appl. Comput. **5**, 423 (2000).

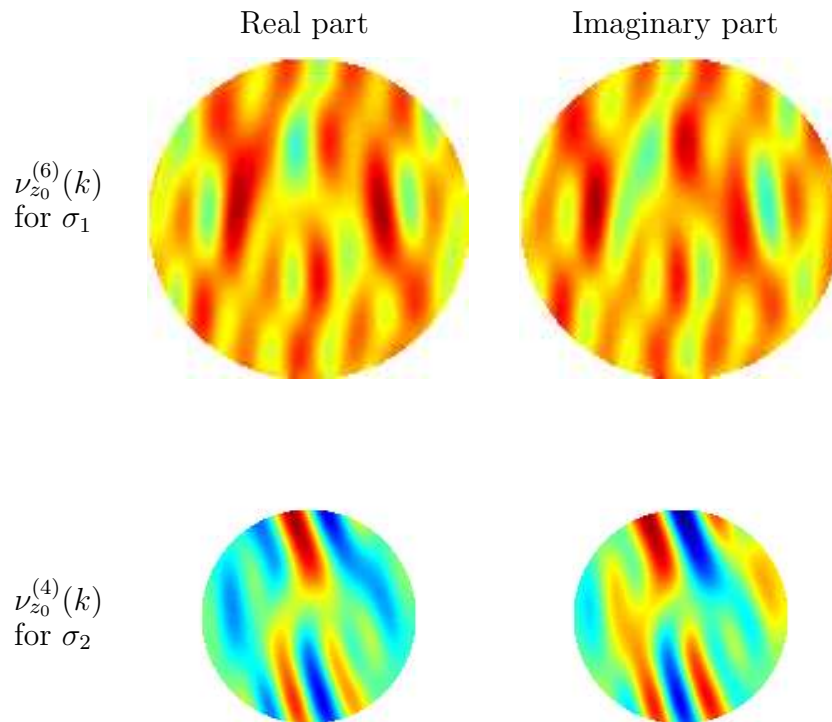


FIGURE 1. Top row: The real (left) and imaginary (right) parts of the function $\nu_{z_0}(k)$ corresponding to the heart-and-lungs phantom σ_1 for $|k| < 6$. Numerical values of the real and imaginary parts range between -0.08 and 0.08 . Bottom row: The real (left) and imaginary (right) parts of the function $\nu_{z_0}(k)$ corresponding to the stratified medium conductivity σ_4 (including the added unit conductivity annulus, see Subsection 6.3) for $|k| < 4$. Numerical values of the real and imaginary parts range between -0.25 and 0.26 . In both cases $z_0 = 1.4$. The colormaps in all four plots are the same, allowing direct comparison of colors (function values).

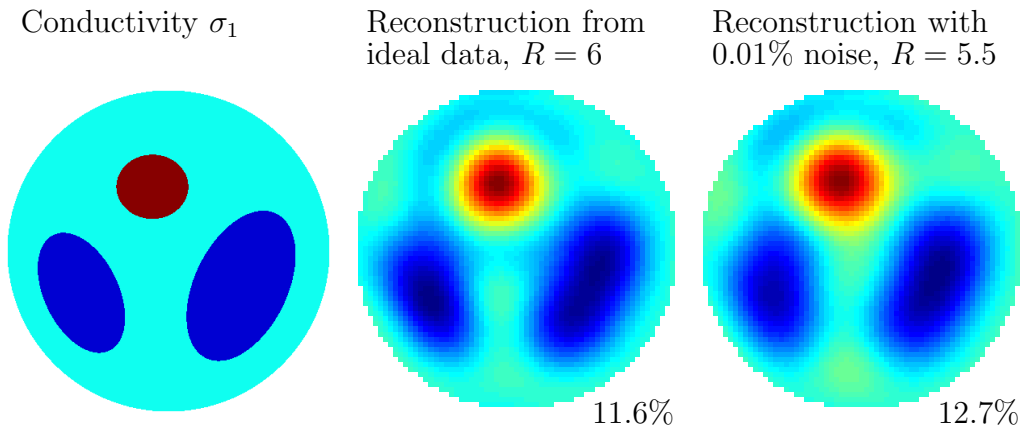


FIGURE 2. Heart-and-lungs conductivity phantom σ_1 and two different reconstructions. The colors (conductivity values) in the three images are directly comparable. The relative error percentages of the two reconstructions are computed using formula (6.1). **Left:** true conductivity σ_1 . **Center:** reconstruction from noise-free data with $z_0 = 1.4$ and cutoff frequency $R = 6$. The minimum conductivity in the reconstruction is 0.637 (true value 0.7); the maximum conductivity is 1.997 (true value 2). **Right:** reconstruction from data with added noise of relative amplitude $\frac{\|E\|_{2,2}}{\|L\sigma\|_{2,2}} \approx 10^{-4}$. Here $z_0 = 1.4$ and the cutoff frequency is $R = 5.5$. The minimum conductivity in the reconstruction is 0.637 and the maximum 1.870.

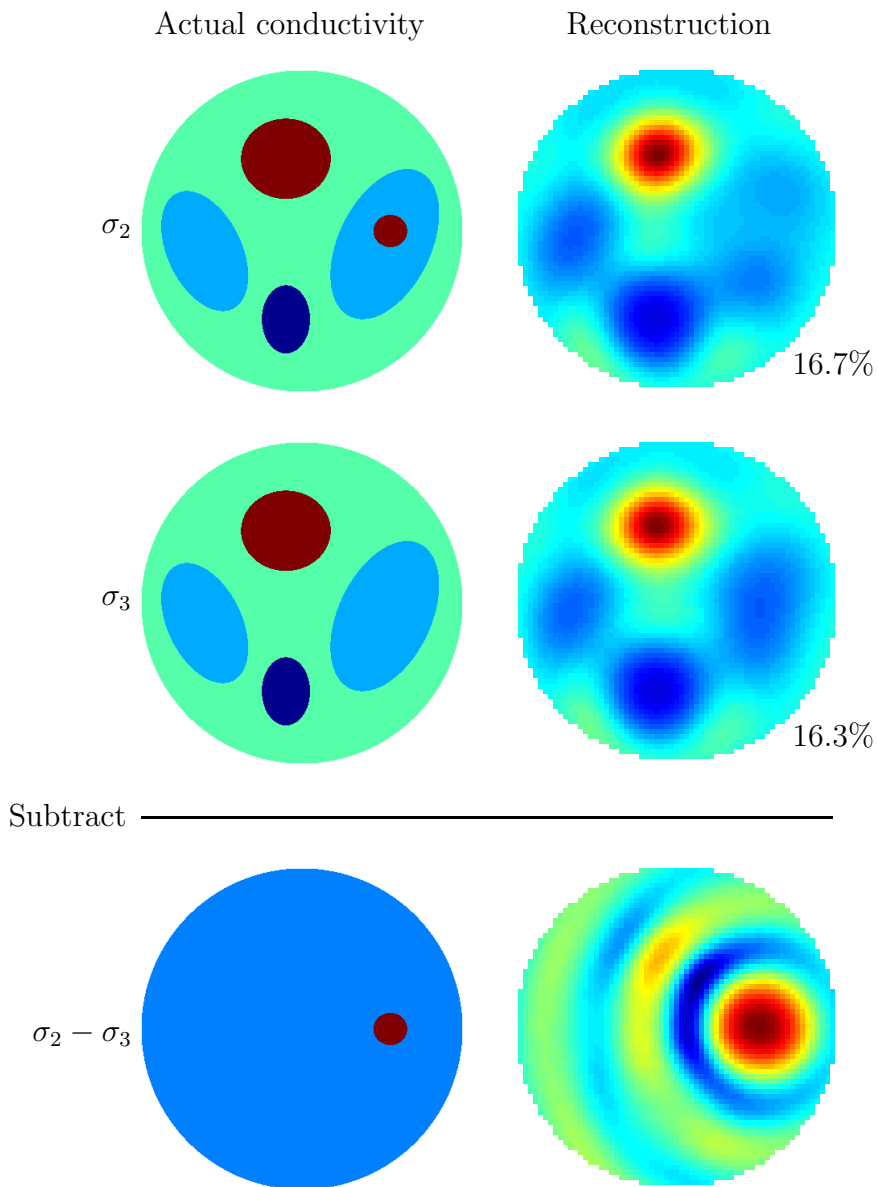


FIGURE 3. True conductivities σ_2 and σ_3 (left) and reconstructions from noise-free data (right). In each case, the cutoff frequency is $R = 5.5$ and $z_0 = 1.4$. The relative error percentages of the two reconstructions are computed using formula (6.1). The bottom row represents a difference image; that is, the reconstruction in the second row is subtracted from the reconstruction in the top row to form the image in the bottom row. In rows 1 and 2, the colormaps in the left and right image are the same. The images in the bottom row are each plotted on their own scale. The true maximum conductivity in the first and second row is 2.0, and the true minimum conductivity is 0.2. The max and min in row one are 2.3319 and 0.3781, respectively. The max and min in row two are 2.2732 and 0.3728, respectively. The true contrast in the difference image is 1.3, while the contrast achieved in the difference image is 0.2073.

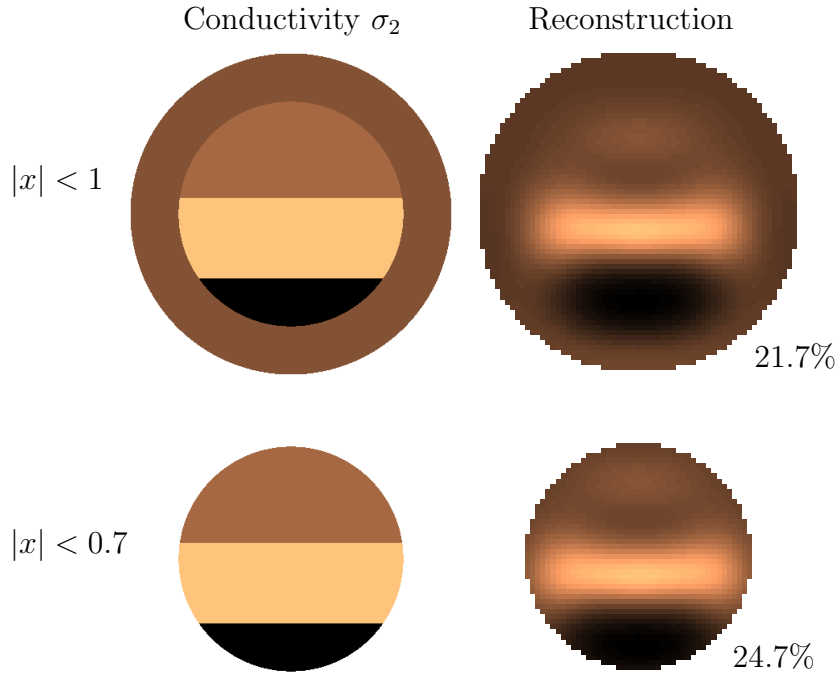


FIGURE 4. Reconstruction of σ_4 using cutoff frequency $R = 6$ and four values of z_0 : real ± 1.4 and purely imaginary $\pm 1.4i$. The four reconstructions have been combined using formula (6.2). In the upper plots the full domain and full reconstruction are displayed; the relative error percentage is computed using formula (6.1). In the lower plots, the outer annulus is removed so that the reconstruction can be analyzed in the region of interest. The relative error percentage 24.7% is computed using formula (6.1) with Ω replaced by the disc $|x| < 0.7$. In the region of interest, the minimum conductivity in the reconstruction is 0.3048, while the true value is 0.3, and the maximum conductivity in the reconstruction is 2.5743, while the true value is 2. The colormaps in all four images are the same, so colors (conductivity values) are directly comparable.